Journal of Inorganic and Organometallic Polymers and Materials
https://doi.org/10.1007/s10904-025-04152-1

RESEARCH

In Situ Synthesis of Anisotropic Silver Nanoparticles on 2D Chitosan Nanosheets: A Polymer-Metal Nanocomposite with Multi-target Genetic Efficacy Against Multidrug Resistant Bacteria

Ola M. El-Borady[1] · **Azza S. El-Demerdash**[2] · **Ahmed S. El Qiey**[3] · **A. El-Shabasy**[4] · **N. T. Abd El-Ghani**[5]

Received: 15 October 2025 / Accepted: 17 December 2025

Abstract

The escalating global crisis of antimicrobial resistance (AMR) necessitates the rapid development of non-traditional, materials-based strategies. Here, we report a simple, one-pot, in situ synthesis of anisotropic silver nanoparticles (AgNPs) directly and uniformly integrated onto the surface of two-dimensional (2D) chitosan (CS) nanosheets. This method exploits the intrinsic reducing and stabilizing capabilities of chitosan, enhanced by a modified synthetic approach using sodium borohydride ($NaBH_4$) at low temperature, to create a robust, synergistic polymer-metal nanocomposite (CS-Ag). Comprehensive characterization (UV–Vis, FTIR, XRD, EDS, HRTEM, AFM) confirmed the successful immobilization and unique morphology, revealing anisotropic AgNPs with an average size of approximately 50 nm uniformly dispersed over the CS nanosheet. Moving significantly beyond standard inhibition assays, this work elucidates the multi-mechanistic and genetic-level action of the CS-Ag nanocomposite against a panel of multidrug resistant (MDR) clinical isolates. The material exhibited exceptional antibacterial potency, with maximum efficacy observed against Gram-negative bacteria, specifically *Enterobacter ludwigii* and *Escherichia coli* O157. To definitively uncover the underlying mechanism, we performed a novel gene expression analysis using a custom qPCR panel. This investigation provided molecular evidence of a multi-pronged attack that simultaneously targets cell structure and genetic defenses: a significant downregulation of key AMR genes (including the beta-lactamase gene (*blaACT*), the efflux pump gene (*acrB*), and the biofilm regulator (*csgD*)). Simultaneously, the bacteria reacted by upregulating genes indicative of cellular stress and repair, such as the heat shock protein gene (*HSP60*) and genes related to cell envelope damage (*uge* and *nhaA*). These compelling genetic findings were rigorously corroborated by molecular docking analysis, which mapped the high-affinity interaction of the nanocomposite with crucial bacterial membrane proteins (such as LolC). Collectively, these results establish the CS-Ag nanocomposite as a high-potential, next-generation hybrid material capable of circumventing and degrading AMR mechanisms by disarming MDR pathogens at the genetic level. This study offers a powerful, data-driven material-science approach for combating antibiotic resistance by simultaneously targeting both cell integrity and genetic defenses.

✉ Azza S. El-Demerdash
dr.azzasalah@yahoo.com; drazza@ahri.gov.eg

[1] Institute of Nanoscience and Nanotechnology, Kafrelsheikh University, Kafr Elsheikh 33516, Egypt

[2] Department of Biotechnology, Agricultural Research Center (ARC), Animal Health Research Institute (AHRI), Zagazig 44516, Egypt

[3] Faculty of Biotechnology, October University for Modern Sciences and Arts (MSA), 6th of October City, Giza, Egypt

[4] Department of Biology, College of Science, Jazan University, P.O. Box. 114, Jazan 45142, Kingdom of Saudi Arabia

[5] Chemistry Department, Faculty of Science, Cairo University, Giza, Egypt

Graphical Abstract

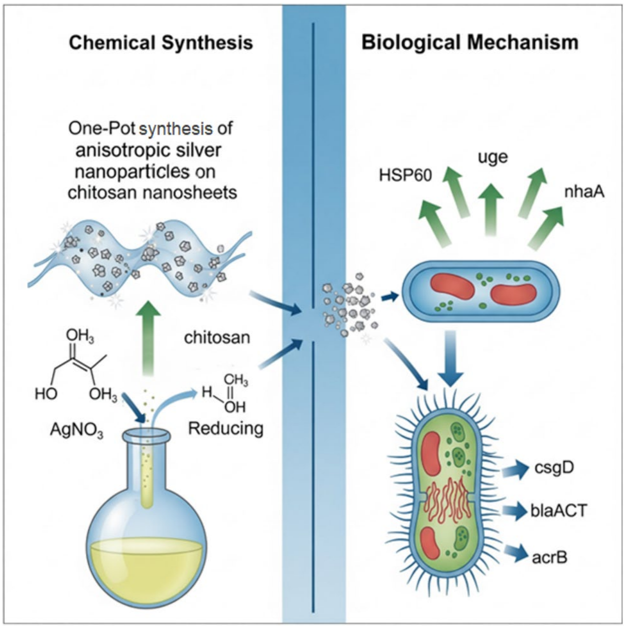

Keywords Anisotropic silver · Chitosan nanosheets · Nanocomposite · Gene expression · Multidrug resistance · Biofilm · Molecular mechanism

1 Introduction

Chitosan (CS) is a versatile polysaccharide that serves as a copolymer of N-acetyl-D-glucosamine and D-glucosamine. It is industrially prepared through the alkaline de-acetylation of chitin, the second most abundant natural biopolymer [1, 2]. Chitosan is highly valued in fields like medicine due to its advantageous intrinsic characteristics, including its superior biodegradability, biocompatibility, and low toxicity, coupled with its relative affordability [3]. Furthermore, it possesses an exceptional ease of chemical modification when compared to other natural biopolymers like chitin, starch, gelatin, and cellulose, allowing for tailoring its functions without negatively affecting its inherent capabilities [4].

A key functional property of Chitosan is its potent and broad-spectrum antimicrobial activity against various microorganisms, such as bacteria, filamentous fungi, and yeast [5, 6]. This antimicrobial potential is particularly significant and applicable within the food chain and bio-security sectors, as it helps control pathogens, thus enhancing food preservation and promoting community health, all without the need for traditional antibiotics. The effectiveness of CS is not static, however, as its antimicrobial action is mediated by a complex interplay of factors, which can be broadly categorized as microbial factors (including the target species and its cellular age), the chemical characteristics of the CS itself (such as its positive charging density, molecular weight, and concentration), its physical condition (including water solubility), and various environmental parameters (such as the medium's pH, temperature, pathogen exposure time, and ionic strength) [7, 8].

The antibacterial behavior of CS is a complex process dictated by the inherent differences in bacterial cell wall structure, particularly between Gram-positive and Gram-negative species. Interestingly, CS is often reported to exhibit a more potent antimicrobial effect against Gram-negative bacteria [9, 10]. The widely accepted primary mechanism is the strong electrostatic attraction between the positively charged CS macromolecules and the negatively charged components of the microbial cell membrane [11]. This binding fundamentally compromises the membrane's integrity, initiating a crucial permeability shift that results in the fatal leakage of essential intracellular contents, such as nucleic acids and proteins, culminating in the complete breakdown of the bacterial cell structure [12]. Furthermore, CS enhances its antimicrobial efficacy by acting as a chelating agent, selectively binding to metal ions and thereby inhibiting the growth and toxin production of microbes [11]. In host tissue, CS also confers protective benefits by functioning as a water-binding agent and an inhibitor for various enzymes [13].

In stark contrast, Silver Nanoparticles (AgNPs) represent a highly effective, new-generation class of antimicrobial agents renowned for their aggressive, broad-spectrum activity [14–16]. AgNPs can effectively inhibit or kill both Gram-positive (such as *Staphylococcus aureus* and *Bacillus subtilis*) and Gram-negative bacteria (*E. coli*), and exhibit significant antifungal activity against various strains, including *Candida* species [17]. Their utility extends beyond bacterial and fungal control, as AgNPs have also demonstrated promising potential against various viruses, such as hepatitis B, respiratory syncytial virus, and monkeypox, with ongoing exploration into their antiviral effect against COVID-19 [18–20]. A critical advantage of AgNPs is their lower propensity to induce microbial resistance compared to many conventional antimicrobials, making them a preferred choice for infection prevention in applications like wound dressings for burns and diabetic ulcers, as well as medical scaffolds [21]. Mechanistic studies, exemplified by investigations into *S. aureus*, indicate that AgNPs damage the bacterial cell membrane, inhibit cellular respiration, and reduce the activity of key enzymes, ultimately leading to microbial cell death [22].

The integration of chitosan and silver into a single nanocomposite (CS-Ag) is a compelling strategy, as it capitalizes on the synergistic effects of both materials to achieve antimicrobial performance superior to either component alone. This versatile platform has garnered significant research attention, not only for its robust antimicrobial effects but also for its broader utility in biomedical applications, including biosensing, wound healing, and cancer therapy [23, 24]. However, the widespread transition of CS-Ag into clinical practice has been significantly hindered by the reliance on traditional multi-step fabrication processes, which are often complex, resource-intensive, and involve the separate synthesis and then combination of the two components.

The present study directly addresses the limitations of multi-step syntheses by pioneering a simple, one-pot, and in situ method for creating anisotropic Silver Nanoparticles (AgNPs) uniformly decorated on Chitosan nanosheets. This novel approach facilitates the large-scale production of the material. Our work comprehensively investigates the resulting material's antimicrobial potential against both Gram-positive and Gram-negative bacteria. Crucially, the research extends significantly beyond conventional minimum inhibitory concentration assays to uncover the underlying molecular mechanisms of action. Utilizing a custom qPCR gene expression panel, we precisely quantify the nanocomposite's influence on key genes associated with antibiotic resistance, virulence factors, and cellular stress pathways. This definitive molecular approach provides a high-resolution understanding of the nanocomposite's efficacy, ultimately positioning this novel CS-Ag material as a promising new tool in the critical global fight against antimicrobial resistance.

2 Material and Methods

2.1 Materials

Chitosan with a medium molecular weight of 190–310 kDa, deacetylation degree of 75–85%, sodium borohydride ($NaBH_4$,≥98.0%) was purchased by Sigma-Aldrich. Silver nitrate ($AgNO_{3,}$ 99,8%), and sodium tripolyphosphate (TPP) were supplied from Merck. Acetic acid (glacial, 99.9%) was purchased from ADWIC, Egypt. Distilled water was used to prepare all aqueous solutions. All the reagents were used as received.

2.2 Synthesis of CS-Ag Nanocomposite

Herein, in situ synthetic procedure was used while the AgNPs were reduced and stabilized over the CS nanosheets through the formation of CS (in the same reaction step) as reported recently [25] with slight modifications. Firstly, the CS solution was prepared by dissolving CS powder (2 g) by stirring in one liter of 1% (w/v) acetic acid until the solution became transparent. Once CS dissolved completely, the CS solution was diluted with distilled water to reach a concentration of 0.01% (w/v) with a pH of 6.0, at 25 °C. Afterthought, 0.5 g of TPP was poured into the CS solution under magnetic stirring at 25 °C and left for an additional 30 min under stirring. The formation of chitosan nanosheets started spontaneously using the TPP-initiated ionic-gelation process (18). Secondly, AgNPs were loaded over the formed CS by adding an aqueous solution of one mM $AgNO_3$ to the CS suspension through its synthesis, followed by adding dropwise an iced solution of 20 mL $NaBH_4$ (0.04 M) with stirring for 1 h. Immediate color changes observed for the solution from white to pale yellow and yellowish-brown indicate the formation of the AgNPs.

2.3 Characterization of the CS-Ag Nanocomposite

The morphological characteristics, including the size and shape of the formed NPs, were determined by the high-resolution transmission electron microscopy (HR-TEM) imaging (JEOL, model JEM-2010, Tokyo, Japan), operated at TEM 200 kV accelerating voltage and attached with Gatan Digital Camera (Model Erlangshen ES500, Japan). For the TEM imaging, the samples were prepared by placing a drop of NPs solution onto carbon-coated copper grids and then were left to dry at room temperature. Then the sample was seen under the microscope. Atomic force microscopy (AFM) was used to provide a topographical, morphological, and confirmed 2D and 3D roughness profile of the particles using AFM (5600LS Agilent Technology Company, Santa Clara, California, USA). 20 µL of the sample was dropped onto a cleaved mica slide and dried at room temperature to generate thin films analyzed in intermittent contact mode. The crystalline and phase structures of the synthesized NPs were examined by an X-ray diffractometer (XRD). The XRD pattern was measured by supporting the sample on a glass substrate and employed with an X-ray diffractometer (BRUKER D8 Discover, Karlsruhe, Germany) in the range of 10 to 90° at a scan rate of 0.02°/min adjusted with the time constant of 2 s. The X-ray source was Cu Kα radiation (k = 1.5406 A°), radiation (applied voltage 40 kV, current 80 mA). The powdered sample of CS powder and CS-Ag nanocomposite elemental composition was detected by energy-dispersive X-ray spectroscopy (EDX) on the scanning electron microscope (SEM), JEOL model JSM-IT100, Japan. The structural information and existence of functional groups were investigated by the FTIR analysis using an FTIR spectrophotometer (JASCO spectrometer, Tokyo, Japan) over the range of 4000 to 400 cm^{-1}. The UV–Vis spectral analysis was followed by measuring the optical absorbance and the plasmonic character of AgNPs solution using spectrophotometer (SHIMADZU RF5301PC double beam, one cm wide quartz cells, Kyoto, Japan). The NPs sample was blended with potassium bromide (KBr) in a 1:100 ratio, compressed to 2 mm disks, and then analyzed.

2.4 The In Vitro Antibacterial Activity

The in vitro antibacterial potential of the prepared CS-Ag nanocomposite and the chemically synthesized AgNPs was tested against four human pathogenic bacteria: two gram-positive bacterial strains (*Bacillus subtilis* and *Bacillus lichniforms*) and two gram-negative bacterial strains (*Escherichia coli* O157 and *Enterobacter ludwigii*). All bacterial strains were provided by the laboratory of microbial genetics, genetic engineering and biotechnology division, national research center, Egypt. The pure cultures of the strains were sub-cultured in Mueller–Hinton broth media and incubated at 35 °C on a rotary shaker at 120 rpm for 24 h. Then, the sub-cultured strains were washed with 0.9% saline solution until obtaining an optical density of 0.5 at 570 nm.

For the Gram-positive strains, *Bacillus subtilis* and *Bacillus licheniformis* were specifically selected as robust environmental and opportunistic pathogen models, possessing the distinct thick peptidoglycan cell wall necessary to evaluate the nanocomposite's ability to penetrate Gram-positive structures, serving as reliable controls for nanoparticle toxicity testing.

Each strain was then swabbed uniformly on individual Mueller–Hinton agar (HiMedia company, Thane (West)—400,604, Maharashtra, India) plates using sterile cotton swabs, and several wells were made on the agar plates using a gel puncher. After that, 100 µL of the samples were added into the respective wells. The samples were left for incubation at 37 °C for 24 h, and the zone of inhibition was measured to indicate the CS-Ag nanocomposite's antibacterial potential on the four bacterial strains [26, 27]. All antimicrobial assays were performed under strict aseptic conditions to ensure plate sterility; plates showing any signs of contamination were excluded and repeated to ensure data integrity.

To quantitatively determine the antimicrobial efficacy, the minimum inhibitory concentration (MIC) was measured using the broth microdilution method In Animal Health Research Institute, Zagazig Branch, Egypt. A series of two-fold dilutions of the CS-Ag nanocomposite were prepared in Mueller–Hinton broth, ranging from 64 to 0.125 µg/mL. Each well was inoculated with a bacterial suspension to achieve a final cell density of approximately 1×10^6 CFU/mL. A positive control (inoculated media without the nanocomposite) and a negative control (sterile media only) were included in each assay. The microplates were incubated at 37 °C for 24 h. The MIC was determined as the lowest concentration of the nanocomposite that showed no visible bacterial growth. Furthermore, a sub-inhibitory concentration (SIC), defined as a concentration equal to 1/2 the MIC, was selected for subsequent molecular analysis. The bacteria were exposed to this Sub-MIC concentration to investigate the molecular mechanisms of action at the genetic level without causing complete cell death. This allowed for the accurate assessment of the nanocomposite's effect on gene expression related to stress, virulence, and antibiotic resistance [28, 29].

2.5 Gene Expression Assay

RNA was extracted from the bacterial cultures using the QIAamp RNeasy Mini Kit (Qiagen). The concentration and purity of the extracted RNA for each sample were measured using a NanoDrop Eight Spectrophotometer (ThermoScientific). The 16S rRNA gene was used as the internal control (housekeeping gene) for normalization.

Primers for all target genes were designed using Primer3 and FastPCR software. Primer sequences are listed in Table 1. The specificity and sensitivity of these primers were optimized and validated through a touchdown PCR protocol and subsequent experimental testing.

Relative quantitative real-time PCR (RT-qPCR) was performed in a 20 µL reaction mixture. Each reaction contained 10 µL of 2 × HERA SYBR® Green RT-qPCR Master Mix (Willowfort, UK), 1 µL of RT Enzyme Mix (20X), 0.5 µL of each primer (20 pmol), 3 µL of nuclease-free water, and 5 µL of RNA template.

The reaction was carried out using a StepOne™ real-time PCR system (Applied Biosystems) following the manufacturer's protocol. The thermal cycling program included an

Table 1 Novel primers for RT-qPCR analysis: sequences and cycling conditions

Target gene	Primers sequences	Amplicon size (bp)	Annealing (°C)	Accession no
E. coli primers				
16S rRNA	F; TGGCGCATACAAAGAGAAGC R; TTTTGCAACCCACTCCCATG	192	58	X80721.1
acrB	F; GGTTCCATCTTCGCCAGTTC R; GCGTGATGTGGCGAAAATTG	159	60	HQ833337.1
csgD	F; GCGACATTGAAAACTGGCCT R; CGATGAGTAAGGAGGGCTGA	190	60	PV012319.1
Enterobacter ludwigii primers				
16S rRNA	F; CTCTTGCCATCAGATGTGCC R; TTCTTCATACACGCGGCATG	201	59	AJ853891.1
blaACT	F; AGAAGTGAACCCTCCTGCTC R; GCGCTCAGAATACGGTATGC	180	60	NG_244411.1
csgD	F; AGAATCGGGTGGTAGAAGGC R; AAACTGAGCATGGGAGACGA	150	60	MT483952.1
HSP60	F; TGCGTCAGATCGTTTCCAAC R; CGGGTCACTTTGGTTGGATC	151	58	MN962910.1
uge	F; TGAGCTGATGTCGCATACCT R; CGATATAGGTGAAGTCGCGC	188	58	MT483961.1
nhaA	F; GGGGCCATCATTATCATCGC R; ATTTCAACACCGCAGTCCAC	169	60	KJ569455.1

initial denaturation step at 94 °C for 15 min, followed by 40 cycles of denaturation at 94 °C for 15 s, annealing at T°C for 30 s, and extension at 72 °C for 30 s. A final extension step at 72 °C for 10 min concluded the reaction.

The cycle threshold (CT) values and amplification curves were generated by the StepOne™ software. Gene expression fold changes were calculated using the $2^{-\Delta\Delta CT}$ method [30, 31] to compare the expression of each target gene in the treated samples relative to the control group. All molecular work was conducted at the Biotechnology Unit, Animal Health Research Institute, Zagazig Branch, Egypt.

2.6 Molecular Docking Analysis

According to Zhou et al. [32]. CS-Ag nanocomposite structure was identified on molecular docking basis. More than 108 structural and functional membrane proteins of *E. coli* were tested in docking analysis. 6F3Z was selected and assessed as the highest proper oriented docking combination. It is protein transport cell membrane that is complex with another periplasmic domain called LolC. The docking procedure was processed by evaluating and rectifying the structural and functional groups of both ligand as Chitosan Ag nanoparticle and receptor site on 6F3Z protein by calculating binding affinity and ligand efficiency through the BIOVIA Discovery Studio Visualizer [33]. The software parameters were conducted by using Auto Dock Tools (v 1.5.6.). It uses the ligands and protein receptors in the PDBQT program format. It adjusts hydrogen on polar and non-polar chemical links besides add and calculate the charges that are suitable for docking analysis. Ligand optimization method includes defining phytochemical component in the 3D conformer downloaded in the form of SDF format. The non-functional groups of ligand that are not participating at docking analysis, they are removed with compensating the electrostatic and unbound energies. Grid box dimensions are determined during Run Auto Grid to obtain the optimization of set map types.

3 Results and Discussion

3.1 The Morphological Studies

The morphological characteristics of the CS-Ag nanocomposite were investigated using HRTEM imaging Fig. 1a, b. The image reveals the formation of chitosan nanosheets. Additionally, the image showed the appearance of AgNPs in distinct anisotropic shapes (spherical, prism, pentagon, and hexagon) with a size around 50 nm in addition to the mostly predominate Ag nanoclusters over CS sheets (size less than 10 nm). The HRTEM image also showed that AgNPs were in an apparent joining to surface boundaries of CS sheets, separated from each other without clumping, and reasonably dispersed, suggesting that CS served as an excellent stabilizing agent [34], preventing the aggregation of AgNPs and helping to narrow size distribution [35]. The selected area electron diffraction (SAED) pattern of AgNPs is showed in Fig. 1c. The ring pattern in SAED further confirms the crystalline nature of the AgNPs. According to the provided in recent work [36], the first strongest ring is the combination of both (111) and (200) planes, whereas the second ring

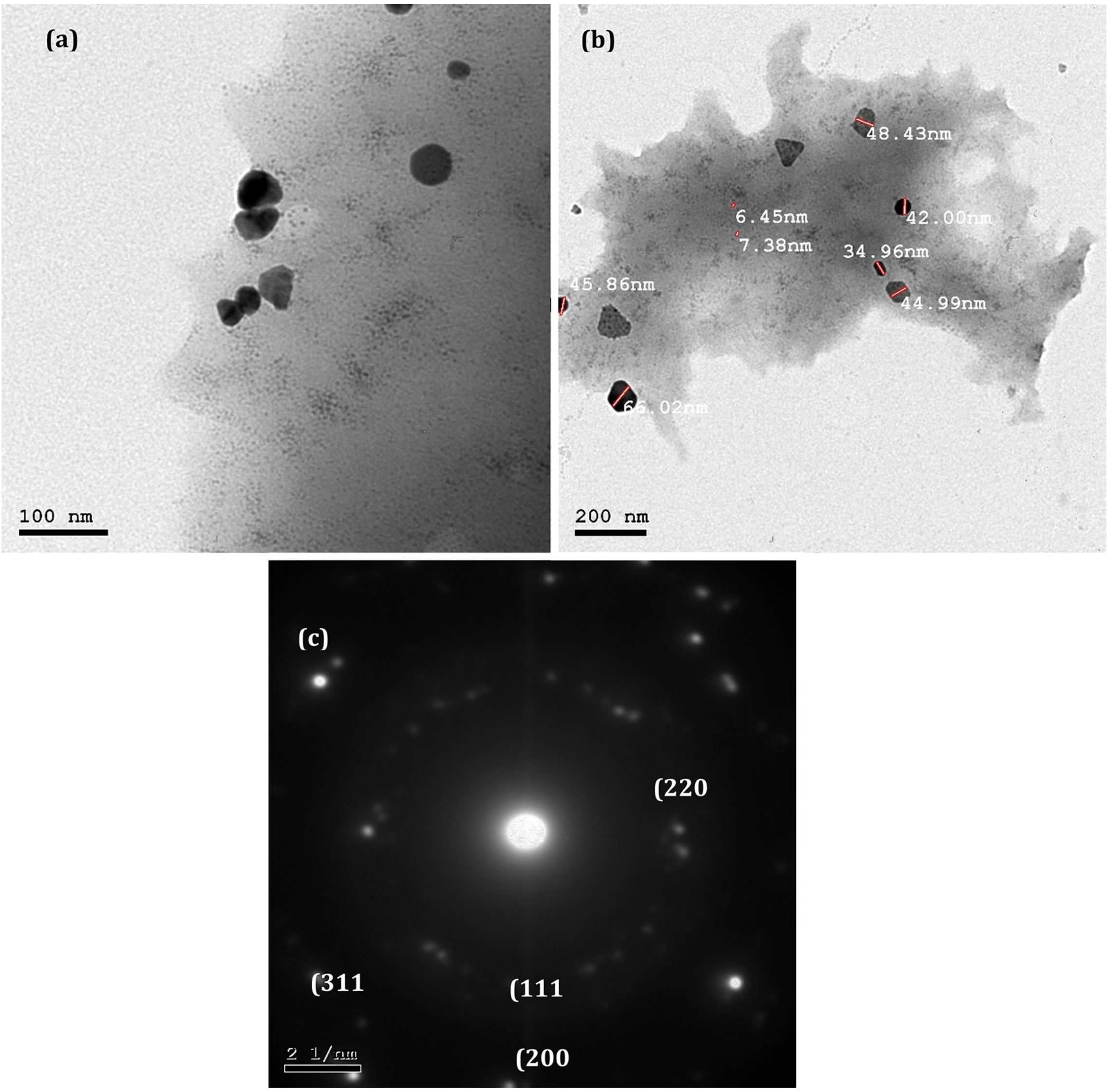

Fig. 1 **a**, **b**, the HRTEM image taken from different spots at various magnifications for the CS-Ag nanocomposite, **c** the selected area electron diffraction (SAED) pattern of AgNPs

corresponds to the crystallographic plane of (220). The third ring represents the Ag's (311) plane, indexed to the face-centered cubic (fcc) structure. The SAED pattern proved that the obtained AgNPs are highly crystalline.

The surface topographical and morphological characteristics of the synthesized CS-Ag nanocomposite were confirmed using the AFM technique. The two-dimensional and three-dimensional AFM images are presented in Fig. 2.

The nanosheet morphology of chitosan is indicated from the 2D and 3D AFM images, which showed broad and planar structures confirming the large, flat, and laterally extended features with smooth topographical transitions as well as the continuous wavy plate-like surfaces Fig. 2a, b, indicating that chitosan forms thin flexible nanosheets rather than discrete particles. This is proved by the low vertical roughness relative to lateral dimensions (Fig. 1 supplemental information). Additionally, as seen from the AFM images, the surface texture appears irregular, indicating crosslinking and dispersion of the AgNPs on the CS surface sheet. Furthermore, the topography pattern in Fig. 2e. Revealed the presence of a high difference around 17 nm, and the existences of discrete nanoscale protrusions (peak height up to 92 nm) along the sheet confirms the successful surface loading of AgNPs on the chitosan surface (Fig. 2a, b, d). The AFM observations are in accordance with the TEM analysis.

3.2 The X-Ray Diffraction (XRD)

The crystallographic and phase structural properties of the synthesized CS-Ag nanocomposite were analyzed using the

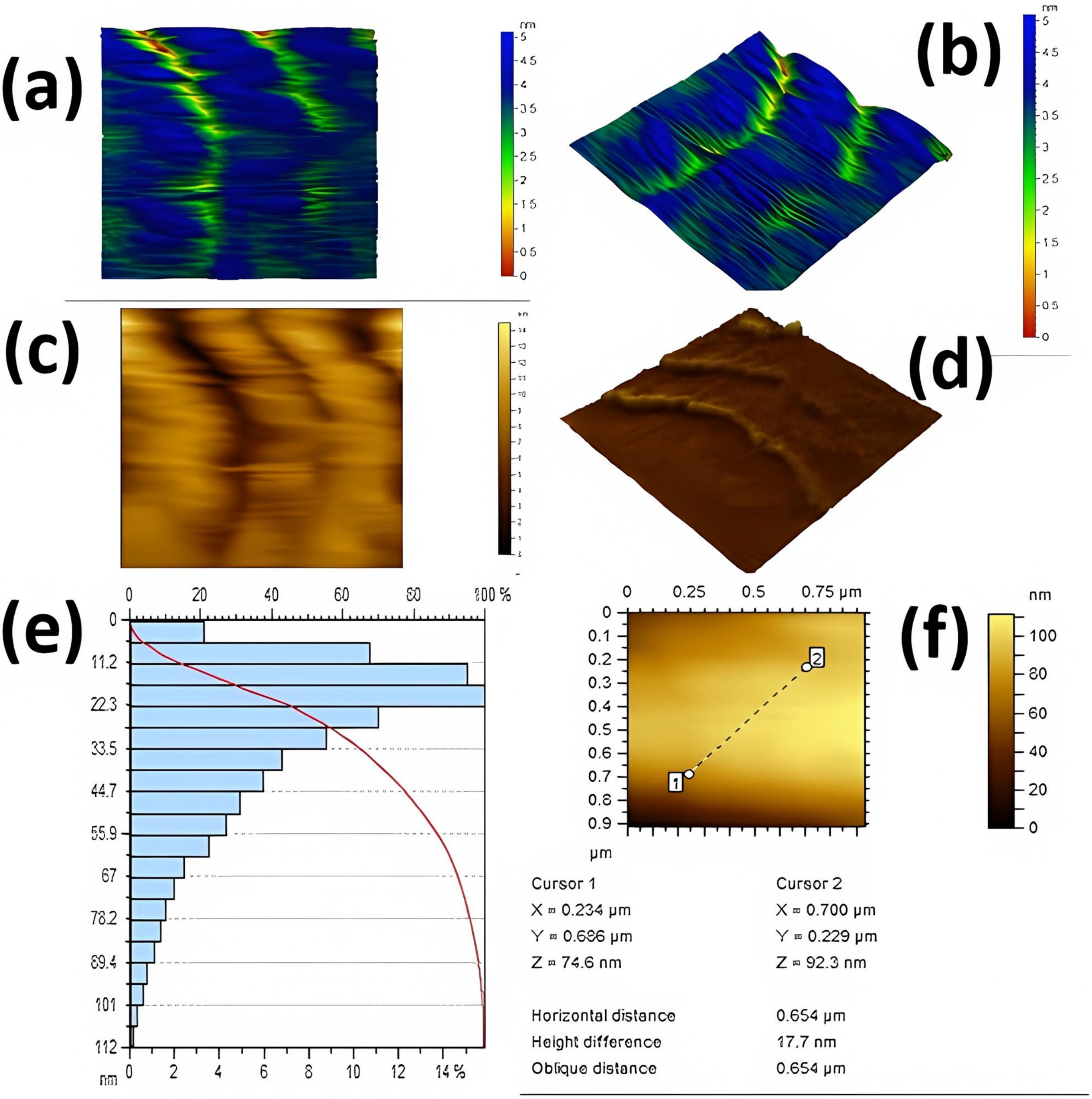

Cursor 1
X = 0.234 µm
Y = 0.686 µm
Z = 74.6 nm

Cursor 2
X = 0.700 µm
Y = 0.229 µm
Z = 92.3 nm

Horizontal distance 0.654 µm
Height difference 17.7 nm
Oblique distance 0.654 µm

Fig. 2 The 2D AFM images from different spots (**a**–**c**), 3D view AFM image (**d**), the topography pattern (**e**), and surface height parameters (**f**) of CS-Ag nanocomposite

XRD technique. The obtained XRD pattern shown in Fig. 3. Appeared in well agreement with the detected data of metallic Ag (JCPDS No. 04-0783) [38]. The diffraction peaks at 2θ = 37.66°, 43.8°, 64.24°, 77.34° corresponding lattice plane value (111), (200), (220) and (311), facets of the face centered cubic crystal structure, respectively. Additionally, the pattern showed the chitosan peaks that represented in an inset pattern and located at 2θ values of 9.50°, 13.50°, 22.50° characteristic for the CS [1]. The presence of the CS peaks with AgNPs peaks in the same XRD pattern proved their combination to form CS-Ag nanocomposite.

The XRD pattern exhibits the more intense peak at 2θ = 43.8°, corresponding to the crystal face of (200), which implying the face-centered cubic crystalline structure of Ag (29). Furthermore, the XRD results proved that the crystalline structure of AgNPs was not changed even after being embedded within CS polymeric matrix [25].

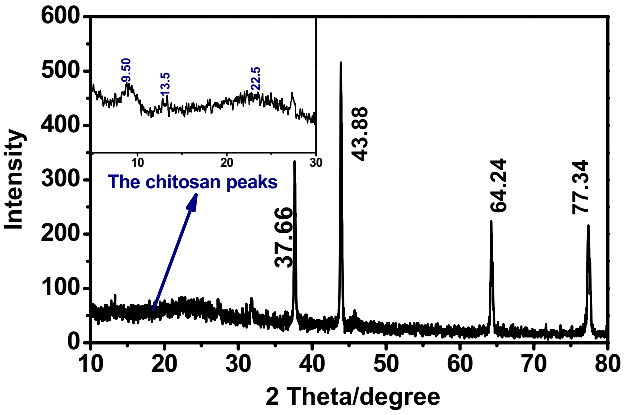

Fig. 3 XRD pattern of CS-Ag nanocomposite

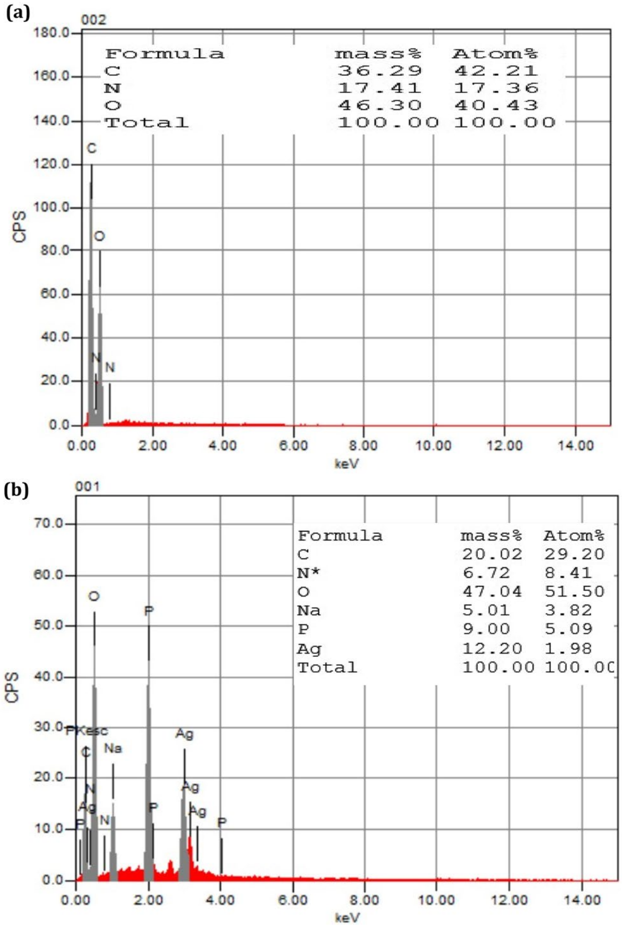

Fig. 4 EDX pattern of (**a**) chitosan bulk and (**b**) the CS-Ag nanocomposite

3.3 The EDX Analysis

The EDX charts for the chitosan bulk and the synthesized CS-Ag nanocomposite are shown in Fig. 4a, b. The EDX chart of chitosan bulk revealed lines for 36% carbon, 46% oxygen, and 17% nitrogen. On the other hand, the CS-Ag nanocomposite EDX analysis confirmed that it contained about 20% of carbon, 47% oxygen, 7% nitrogen, and a distinct signal and high atomic percent values of 12% silver, implies the presence of silver on chitosan.

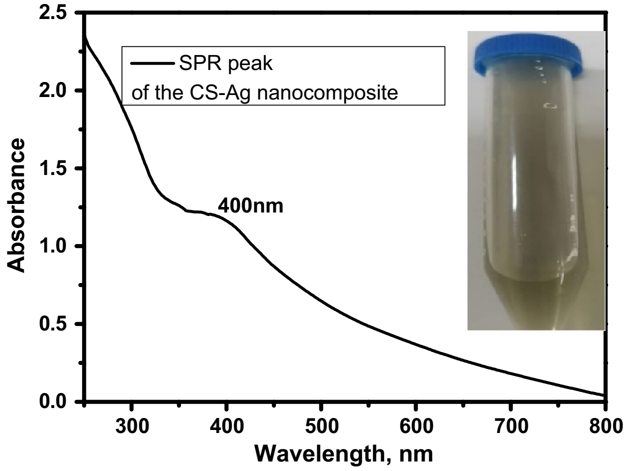

Fig. 5 UV–Vis absorption spectra of CS-Ag nanocomposite showing the surface plasmon resonance (SPR), and the inset is its photo image

3.4 The Spectral Analysis

3.4.1 The UV–Vis Spectral Study

The UV–Vis absorption spectrum of CS-Ag nanocomposite is depicted in Fig. 5. The maximum absorption peak was displayed around 400 nm, due to the surface plasmon resonance (SPR) of AgNPs [37], this peak is characteristic for the AgNPs, indicating its formation over the CS sheets. The obtained UV–Vis absorption results are matched with the recorded later [38].

The stability strength of CS-Ag nanocomposite was also established by measuring the absorption spectrum of the prepared sample after two weeks. No significant changes were observed in its UV–Vis absorbance and no visual change in the solution color during the storage time, demonstrating that the CS-Ag nanocomposite was stable during this period and did not agglomerate.

3.5 The FTIR Analysis

The FTIR analysis of CS bulk and the synthesized CS-Ag nanocomposite were performed to characterize their chemical structure and investigate the linkage functional groups in CS that may bond to the AgNPs Fig. 6a. The FTIR spectrum of CS showed a peak at 3,436 cm^{-1} due to the stretching vibration of the OH or NH-amine in amino groups [39, 40]; this band appeared wider, with a noticeable lowering in its wavelength (at 3,428 cm^{-1}) in the spectrum of CS-Ag nanocomposite indicating its contribution as an active site for

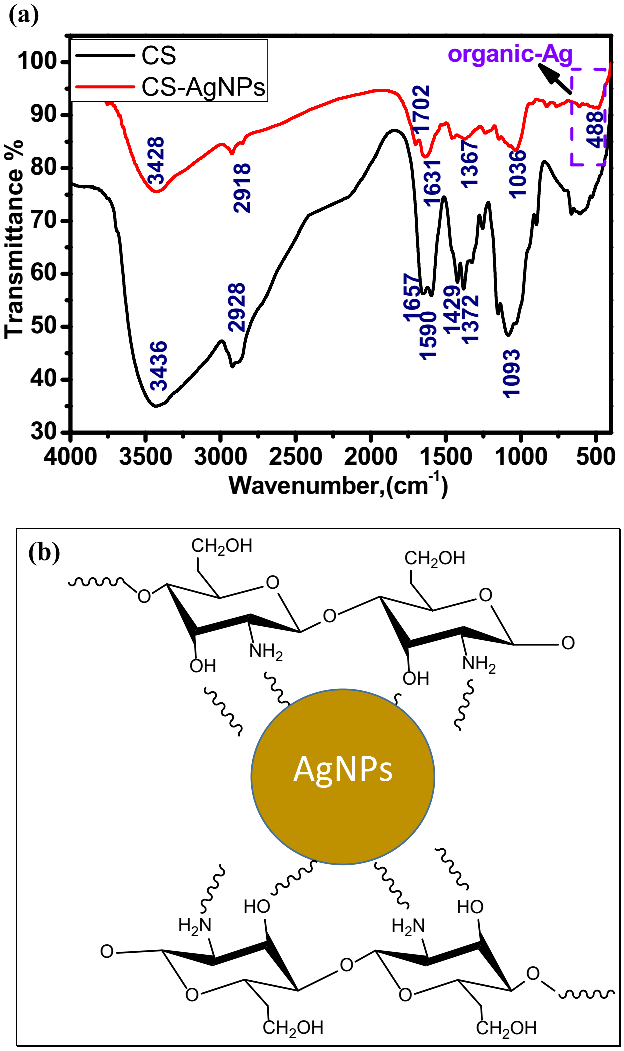

Fig. 6 (**a**) the FTIR of the bulk CS and the synthesized CS-Ag nanocomposite, (**b**) is a schematic diagram showing the mechanism of the interaction of CS matrix with AgNPs

the interaction and linkage of AgNPs to CS through these groups [1]. Additionally, the C–H and C–N stretching peak at 2,920 cm^{-1} in CS appeared shorter and slightly lowered in its wavelength; around 2,918 cm^{-1} in CS-Ag nanocomposite, evidence that it is affected by the presence of silver on chitosan. The N–H bending group of amide is characterized by peaks in the range from 1600 cm^{-1} to 1700 cm^{-1}; in the present work, the CS showed this peak at 1,657 $cm^{-1}$and at 1,702 cm^{-1} for CS-Ag nanocomposite; additionally, the N–H angular deformation in CO NH_2 plane appeared at 1,590 cm^{-1} of CS and 1,631 cm^{-1} for CS-Ag nanocomposite; the redshift and changes in the N–H peaks of CS compared to the N–H peaks in nanocomposite confirm the NH group's role in the interaction between CS and AgNPs. Furthermore, the peak at 1093 cm^{-1} in the IR chart of CS is assigned to the protein stretch carbonyl C–O–C stretching presented in CS [41]; this peak was presented at a lower wavelength, 1038 cm^{-1} in the IR chart of CS-Ag nanocomposite with an observed decrease in its intensity indicating its effect due to the interaction between the AgNPs and CS surface. The peak located at 488 cm^{-1} in the IR chart of the nanocomposite may be attributed to the organic-metal bond [42]; this peak was not observed in the IR chart of free CS, which confirms the presence of AgNPs on the CS matrix.

Based on FTIR findings, it is demonstrated that the OH and the $–NH_2$ groups of CS may be considered as binding sites that have bound with Ag^0 creating the CS-Ag nanocomposite. Figure 6b suggested interaction of Ag with electron-rich oxygen and nitrogen atoms of polar hydroxyl and amide groups of CS, leading to effective stabilization and assembly of AgNPs on the polymeric medium of CS [41].

3.6 Formation Mechanism of CS-Ag Nanocomposite

The current study discussed the *in-situ* syntheses of AgNPs incorporated into the biodegradable polymer's chitosan nanosheets by utilizing $AgNO_3$ as a metal precursor, $NaBH_4$ as a reducing agent, and the chitosan as a stabilizing agent. After adding the $AgNO_3$ and $NaBH_4$ to the formed chitosan nanosheets in its reaction media through chitosan nanosheets preparation, a redox reaction starts on the surface of the chitosan nanosheets while the Ag^+ is reduced to form Ag^0. At this moment, the active functional groups [43] (amine and hydroxyl groups as indicated from the FTIR results Fig. 6) of chitosan start to climb the Ag^0 onto its surface, i.e., stabilize the formed NPs from aggregation, which arises from the polymeric network's steric stabilization and bulkiness of the CS matrix. Additionally, the color change observed for the CS nanosheets solution from the turbid white color to yellowish-brown upon adding $NaBH_4$, indicates the perfect immobilization of AgNPs. A previous study [44], reported that the chitosan behaves like a cationic polymer in acidic conditions derived from the amino group's protonation.

The current progress is in the synthesis of AgNPs as nanocrystals based on a bottom-up approach with precise shape, size, and structure is managed by the nucleation and growth development processes. The first model that provided insight into precursor decomposition and reduction, nucleation, development into seeds, and ultimately growth into nanocrystals in solution was LaMer's group theory [45]. This theory suggests the development of the seeds and surfactant reactivity with certain nanocrystal facets determine the overall shape and size of the nanocrystals; while the surfactants like $NaBH_4$ are typically utilized as reducing agents [46, 47]. According to LaMer's model, the precursor initially decomposes and elevates its ions, which are subsequently reduced into atoms in the solution up to a supersaturation points (S. point), (step I). During this step, the precursor is split into monomeric or/and larger units by creating compounds with surfactant, anions, and solvents molecules [46, 48], following that the formation of tiny clusters, the nucleation process, (step II). Once the burst nucleation begins, the supersaturation concentration reduces because the nuclei develop more quickly than the precursors decompose. The self-aggregation/nuclei production process is slowed down to the minimal S. point, and growth begins with atomic addition (by diffusion) (step III). The genesis of the seeds, such as single, twinned, or multiply twinned structures, begins below the minimal S. point, and it is subsequently converted to a single crystal based on oxidative etching. In comparison to a single crystal, the twinned, stacking faults, and boundary defect accompanying formations have a larger oxidative surface environment that is significantly impacted by oxidative etching.

Nanocrystals can be formed into precise shapes by manipulating a number of thermodynamic and kinetic factors [49]. The most frequent factor in both thermodynamic and kinetic material synthesis is temperature, with kinetic reaction taking place when the temperature is decreased and thermodynamic reaction taking place when it is increased. It is indicated that the {111} facet of the face-centred cubic (fcc) structure (either octahedral or tetrahedral structure) has a larger surface area than the {100} and {110} facets and significantly reduces the system's overall energy [49]. However, if the decomposition or/and reduction rate is extremely slow., the kinetics regulated reaction effects, so the dominance of the twinned, or multiply twined, and stacking fault's structure is in opposition to the thermochemical regulated routes. This is what occurred in the current study, as the Because the nucleation reaction for creating AgNPs was carried out in a low-temperature, ice-path environment, thus the preferred reaction is kinetics-controlled reaction that cause the formation of thee twinned, or multiply twined AgNPs (anisotropic shapes).

Moreover, we demonstrate that on lowering the chitosan pH from neutral to acidic conditions (At pH 4.0), it gradually transforms from the aggregation form to the stiff chains, while the glucosamine residues included in the chitosan polymer are almost entirely protonated, which may deliver some stiffness and stretching of the flexible chains due to the mutual electrostatic repulsion accordingly, the chitosan act as a stabilizing agent, and may easily interact more strongly with the (111) planes of the AgNPs facilitating the formation of AgNPs plates shapes rather than spherical shape.

3.7 The Antibacterial Assessment

The CS-Ag nanocomposite was investigated against two different Gram-positive bacterial strains (*Bacillus subtilis* and *Bacillus licheniformis*) and two Gram-negative bacterial strains (*Escherichia coli* and *Enterobacter ludwigii*). The test was employed using the agar well diffusion method. To further evaluate the sample's effectiveness, a comparison was made with a sample containing the prepared CS-Ag nanocomposite supplemented with chemically prepared AgNPs according to our previously optimized borohydride reduction method [37] (CS-Ag nanocomposite/AgNPs). The primary results are represented in Fig. 7, and their inhibition zone values are listed in Table S1 (Supplemental Information).

The CS-Ag nanocomposite demonstrates potent, broad-spectrum antibacterial efficacy against all tested microorganisms. The two strains exhibiting the highest sensitivity were identified as *Enterobacter ludwigii* (16.44 mm) and *Escherichia coli* (14.82 mm).

The Minimum Inhibitory Concentration (MIC) values confirm this trend, with the nanocomposite inhibiting Gram-negative bacteria at significantly lower concentrations (0.25 μg/mL for *E. coli* and 0.5 μg/mL for *Enterobacter ludwigii*) compared to the Gram-positive strains (8 μg/mL and 16 μg/mL). This highlights a superior and promising activity against Gram-negative pathogens, which are often structurally more resistant and difficult to treat. These antibacterial results are in agreement with earlier findings [50].

The proposed antibacterial mechanism for the prepared nanocomposite involves a multi-pronged attack. The positively charged chitosan (CS) matrix initiates the process by acting as a powerful electrostatic attractor for the negatively charged bacterial surface. This enhanced efficacy against Gram-negative bacteria is attributed to the presence of the cationic NH_3^+ group of the glucosamine monomer in the CS surface, which effectively interacts with the highly anionic Lipopolysaccharide (LPS) layer of the Gram-negative cell wall (electrostatic attraction) [51–54]. This binding disrupts the outer membrane, constructing pores and facilitating the internalization of the AgNPs, constantly leading to the rapid damage of bacteria and altering cell permeability [55].

Additionally, the presence of AgNPs in the nanocomposite has a significant contribution as an antibacterial agent. While, AgNPs may release Ag ions from NP surfaces, that may be accompanied by the interaction of Ag^+ with cellular targets leading to bacterial death [56]**.** Nevertheless, some studies had reported that the AgNPs toxicity towards bacterial growth might arise from the direct physical processes of nano objects, such as cell membrane disruption, interaction with the bacterial ribosome, or the NPs penetration into the cytoplasm [57, 58]. The current results are in consistent with the data observed with previously reported studies [1, 59–61] tested the antimicrobial activity of CS-Ag nanocomposite against *S. aureus* and *Salmonella entrica*. This efficacy is particularly relevant given the urgent clinical need for agents effective against persistent pathogens like MRSA

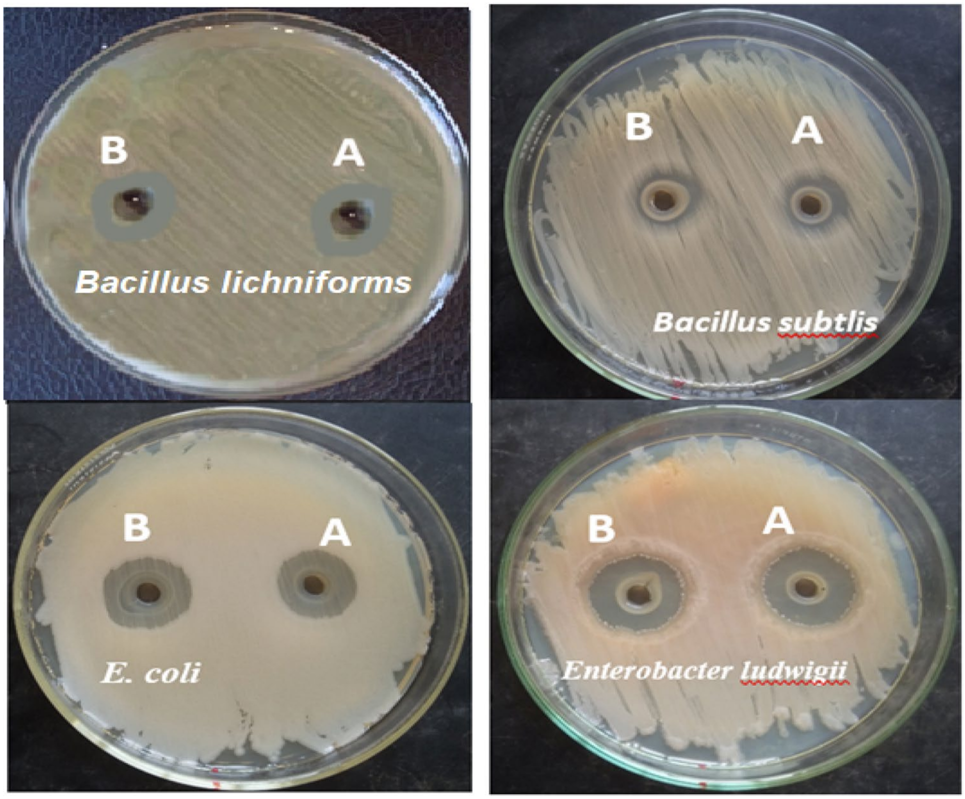

Fig. 7 Antimicrobial activity of CS-Ag nanocomposite (A), and CS-Ag nanocomposite added to AgNPs chemically prepared (B) evaluated by well diffusion method against selected microorganisms

in chronic infections, a need actively being addressed by recent research into AgNPs within hydrogel systems for accelerated diabetic wound healing [62, 63].

Another crucial mechanism is associated with the CS-Ag nanocomposite being transported to the intracellular matrix by proteins found on the outer surface of Gram-negative bacteria. The interaction between chitosan and cellular DNA causes the inhibition of the transcription of DNA, RNA, and protein synthesis, ultimately leading to cell death [64]. The promising therapeutic potential of AgNPs in combating drug-resistant bacteria and expediting wound recuperation is widely supported, whether the nanoparticles are synthesized through phytogenic or chemogenic routes [54, 62] Our study contributes to this growing field by demonstrating a high-resolution mechanistic analysis of a highly potent chemogenic CS-Ag hybrid. The proposed antibacterial mechanisms of CS-Ag nanocomposite is illustrated in Fig. 8.

3.8 Gene Expression Findings

To comprehensively understand the mechanism of the CS-Ag nanocomposite's action, we performed a quantitative gene expression analysis (qPCR) on a custom panel of genes in *E. coli* O157 and *Enterobacter ludwigii*. Our findings reveal a sophisticated, multi-mechanistic attack by the nanocomposite that simultaneously inhibits key bacterial defenses while inducing a severe stress response. The results of the relative gene quantification are summarized in Figs. 9, 10.

3.8.1 Downregulation of Resistance and Virulence Genes

The most significant finding is the nanocomposite's ability to severely downregulate genes associated with antibiotic resistance and virulence, effectively disarming the pathogen.

1. *blaACT* gene: The expression of the *blaACT* gene, which encodes a Class C AmpC β-lactamase, was significantly downregulated in treated *Enterobacter ludwigii*. These β-lactamase enzymes are a primary mechanism of resistance to β-lactam antibiotics, which are a major class of clinical drugs [65, 66]. The nanocomposite's ability to silence this gene suggests it could restore the efficacy of these antibiotics and potentially overcome existing resistance in pathogens.
2. *acrB* gene: The *acrB* gene, a key component of the AcrAB-TolC efflux pump system, was also substantially downregulated in treated *E. coli*. The AcrAB-TolC pump actively expels a wide range of antibiotics and other antimicrobial compounds from the cell, making it a central pillar of multidrug resistance [67, 68]. The observed gene silencing indicates the nanocomposite's efficacy is linked to its ability to disrupt this crucial resistance mechanism, preventing the bacterium

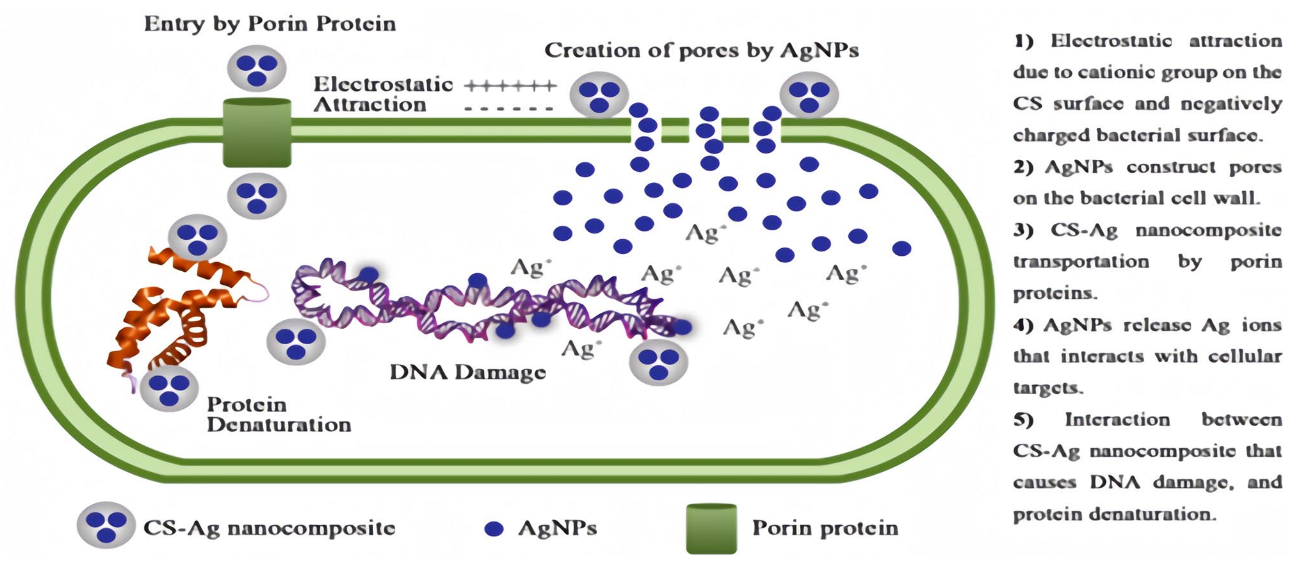

1) Electrostatic attraction due to cationic group on the CS surface and negatively charged bacterial surface.
2) AgNPs construct pores on the bacterial cell wall.
3) CS-Ag nanocomposite transportation by porin proteins.
4) AgNPs release Ag ions that interacts with cellular targets.
5) Interaction between CS-Ag nanocomposite that causes DNA damage, and protein denaturation.

Fig. 8 Schematic represents the different antimicrobial activity mechanisms of CS-Ag nanocomposite

Fig. 9 The mRNA Expression of Key Virulence Genes in *E. coli* After CS-Ag Nanocomposite Added to AgNPs Chemically Prepared Treatment

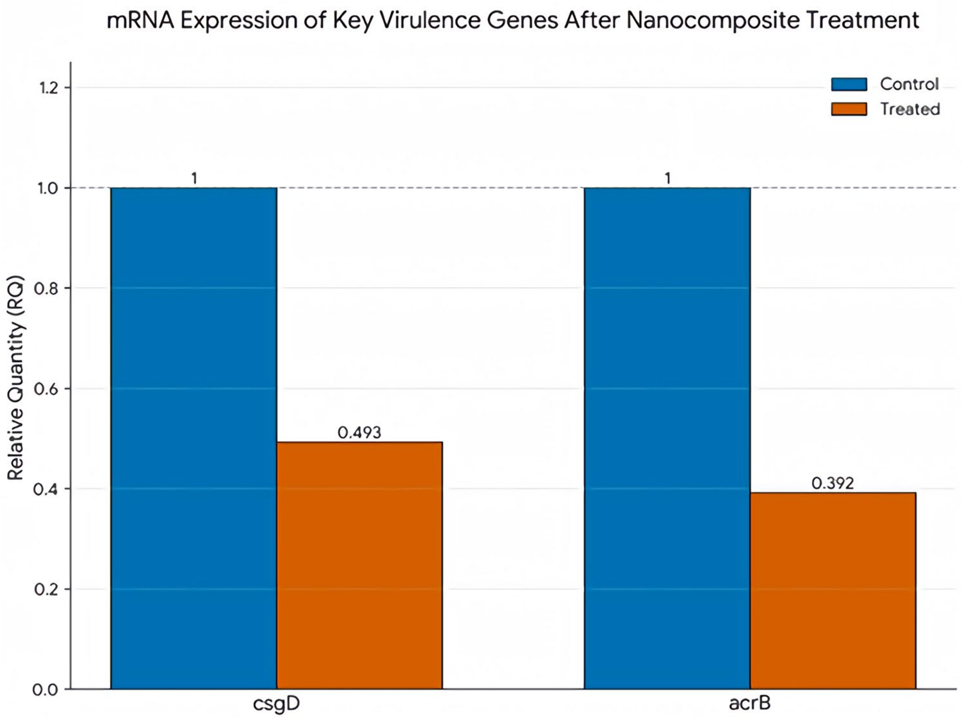

from actively pumping out the silver and other potential antimicrobials.

3. *csgD* gene: Expression of the *csgD* gene, which acts as a master regulator for biofilm formation, was significantly downregulated in both *E. coli* and *Enterobacter ludwigii*. Biofilms provide bacteria with a protective fortress, making them thousands of times more resistant to antibiotics and disinfectants [69–71]. By inhibiting the expression of *csgD*, the nanocomposite prevents the formation of these protective structures, leaving the bacteria vulnerable and providing a crucial pathway to overcoming their natural defenses.

3.8.2 Upregulation of Stress and Survival Genes

In contrast to the downregulation of defense genes, the nanocomposite also induced a powerful stress response in the bacterial cells, evidenced by the significant upregulation of several genes in treated *Enterobacter ludwigii*. This represents the bacterium's desperate attempt to survive the

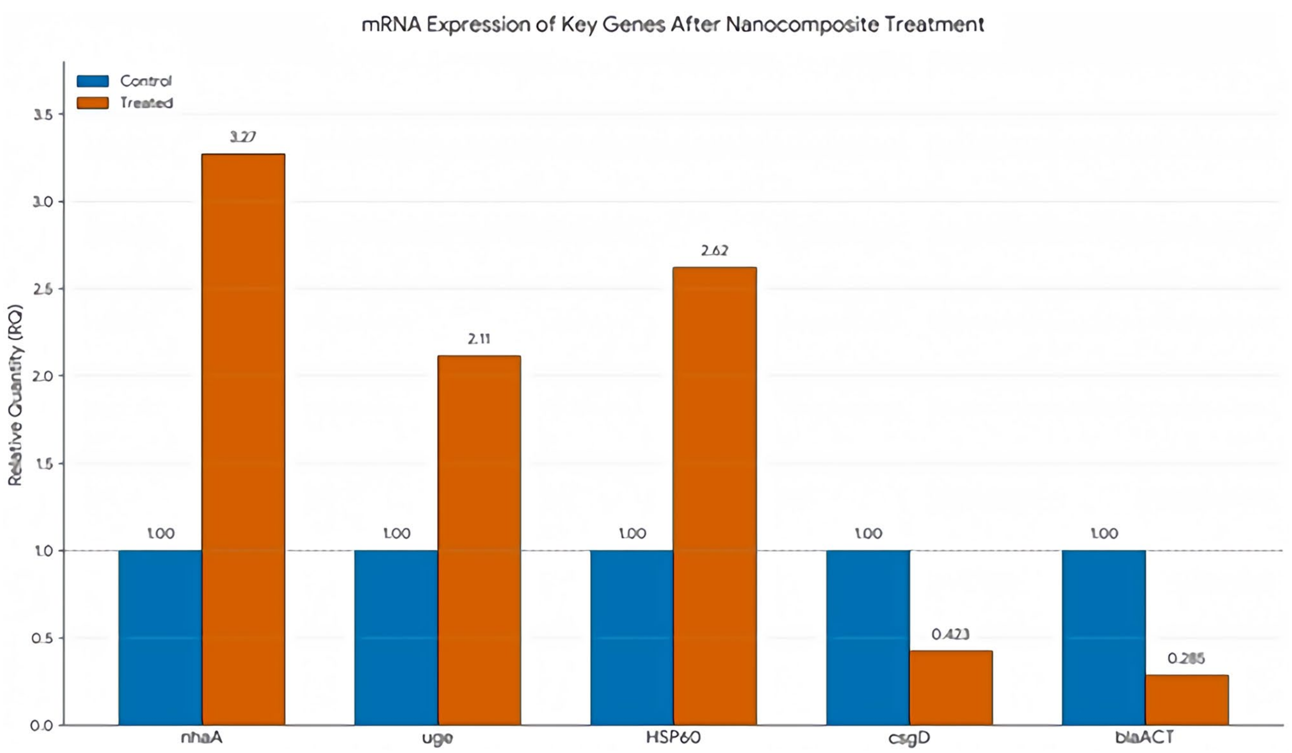

Fig. 10 Relative Quantification of Gene Expression in *Enterobacter ludwigii* Treated with CS-Ag Nanocomposite Added to AgNPs Chemically Prepared Nanocomposite

severe assault. The three most significantly upregulated stress-related genes were *nhaA, HSP60,* and *uge.*

1. *nhaA* gene: The *nhaA* gene, which encodes a sodium-proton antiporter, was highly upregulated. This protein is critical for maintaining the bacterium's internal ionic balance and pH homeostasis [52]. The substantial increase in its expression signifies that the nanocomposite severely compromises the cell membrane and its proton motive force, forcing the cell to invest significant energy into repairing its critical ionic gradients to prevent collapse.
2. *HSP60* gene: The *HSP60* gene, a chaperone protein involved in the general heat-shock and stress response, was also upregulated. This indicates that the nanocomposite's multi-pronged attack—likely involving oxidative stress, membrane damage, and protein denaturation—triggers a broad cellular stress response [53]. The upregulation of *HSP60* is a classic sign that the cell is under immense duress and is scrambling to refold damaged proteins and maintain cellular function.
3. *uge* gene: The *uge* gene, crucial for the synthesis of lipopolysaccharide (LPS) and other polysaccharides in the outer membrane of Gram-negative bacteria [54], was upregulated. This upregulation suggests that the nanocomposite causes significant damage to the bacterial cell wall and outer membrane. The cell responds by drastically increasing the expression of this gene in a futile attempt to repair and rebuild its compromised protective barrier.

3.8.3 The Molecular Docking Results: Linking Structure to Gene Expression

Molecular docking analysis was performed to computationally investigate the potential binding mechanisms of the CS-Ag nanocomposite with key structural and functional surface proteins of *E. coli*. This approach complements our experimental findings by providing a theoretical basis for the observed antimicrobial effects.

Our docking results identify the lipoprotein-releasing system transmembrane protein LolC and the outer-membrane lipoprotein carrier protein as the most favorable binding targets. The nanocomposite exhibited a strong binding affinity within the active site of the 6F3Z protein complex. This protein complex is an asymmetric hetero-2-mer macromolecule, where Chain A is the lipoprotein-releasing system transmembrane protein LolC (responsible for 4 genes) and Chain B is the outer-membrane lipoprotein carrier protein (responsible for 5 genes) (Table 2, 3 Supplemental Information) and Fig. 11 [72].

This computational evidence provides a compelling explanation that integrates our genetic and biochemical findings. The LolC protein is an essential component of the

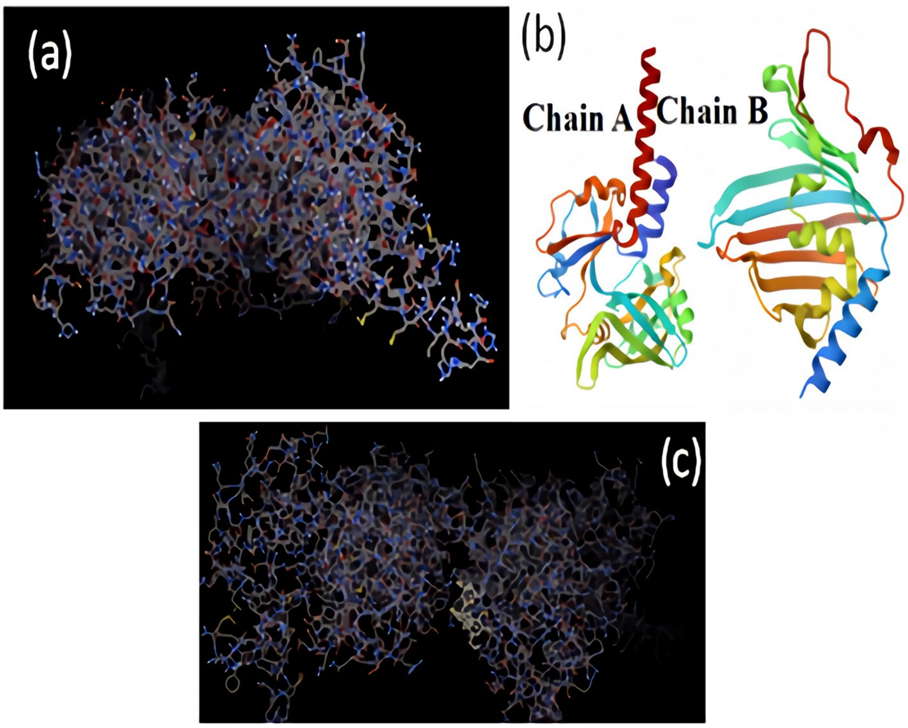

Fig. 11 **a**, 6F3Z protein structure, red bonds; amino acids residues, green bonds; carbon carbon bonds, blue bonds; polar bonds, while bonds; Sulphur Sulphur bonds, **b** Chain A and chain B for 6F3Z protein expression, **c** Docking between Protein and ligand

LolABCDE system, which is responsible for the crucial trafficking and localization of outer membrane lipoproteins necessary for bacterial viability. The high-affinity binding and proposed denaturation of the LolC/LolCDE complex by the CS-Ag nanocomposite directly inhibit essential energy transport and disrupt cell envelope formation.

The resulting molecular-level disruption of the outer membrane barrier is consistent with the exceptionally large inhibition zones observed in our study (30 mm) against *E. coli* O157). Furthermore, and critically, this binding directly supports our gene expression data:

The disruption triggers the cell's urgent response to repair its compromised cell envelope, evidenced by the significant upregulation of the *nhaA* and *uge* genes (as LolC disruption causes hydrolysis of nucleotide binding domain from *nhaA* and *uge* genes mentioned in literature [72]).

The generalized damage leads to protein misfolding stress, which correlates with the upregulation of the *HSP60* gene.

Thus, the docking result (binding to LolC) identifies the initial high-affinity target that ultimately cascades into the observed genetic stress response (*nhaA, uge, HSP60*) and confirms that the nanocomposite's primary point of attack is the bacterial cell membrane, leading to a fatal energy imbalance.

4 Conclusion

This research demonstrates a significant advancement in the synthesis of functional nanomaterials through a simple, one-step, in situ approach. The ability to perfectly immobilize anisotropic silver nanoclusters directly onto chitosan nanosheets represents a creative and efficient fabrication method, eliminating the need for complex, multi-step processes. This unique nanoscale architecture, where the polymer matrix serves as both a scaffold and a stabilizing agent, is central to the material's exceptional performance.

The profound antimicrobial efficacy of this nanocomposite, with a 30 mm inhibition zone against highly resistant pathogens, is a direct consequence of this bespoke material design. The high surface area and unique morphology of the anisotropic silver nanoclusters, in combination with the biocompatible chitosan platform, enable a multi-mechanistic attack on the bacterial cell. This study provides a molecular blueprint of this action, revealing the material's ability to simultaneously induce a cellular stress response by upregulating genes like *HSP60* and *nhaA*, while also dismantling the pathogen's defense system through the downregulation of key resistance and virulence genes such as *acrB, blaACT,* and *csgD*.

Finally, this work is a powerful demonstration of how creative nanomaterial design can lead to breakthroughs in function. We show that by engineering a nanoparticles-polymer composite, we can create a powerful antimicrobial agent that not only kills but also genetically disarms pathogens. This strategy represents a promising new direction in the development of materials for combating the global crisis of antimicrobial resistance.

Supplementary Information The online version contains supplementary material available at https://doi.org/10.1007/s10904-025-04152-1.

Acknowledgements Hereby, Authors of this research would like to appreciate and Acknowledge Prof. Dr. Ayman Diab and Prof. Dr. Gehan Safwat (the Dean and Vice dean of Faculty of Biotechnology, October University for Modern Sciences & Arts (MSA), Egypt) for their support.

Author Contributions O.M.E-B. conceived the original idea, designed and performed the nano-experimental work, executed the characterization, and interpreted the results. A.S.E-D. conducted the bacteriological and molecular assays, handled the software and visualization tasks, validated the results, and contributed to the writing of the manuscript. A.S.E. carried out the experimental work for antimicrobial activity and assisted with the nano-preparation. A.E-S. performed the molecular docking analysis and interpreted its results. N.T.A. revised the manuscript's final form, specifically the nano-synthesis section. All authors reviewed and approved the final version of the manuscript.

Funding Open access funding provided by The Science, Technology & Innovation Funding Authority (STDF) in cooperation with The Egyptian Knowledge Bank (EKB). The authors did not receive support from any organization for the submitted work.

Data Availability All data used have been included in this research article and its supplementary information files.

Declarations

Conflict of interest The authors declare no competing interests.

References

1. S. Govindan, E.A.K. Nivethaa, R. Saravanan, V. Narayanan, A. Stephen, Appl. Nanosci. **2**, 299 (2012)
2. N.M. Ali, G.A.E. Mohamed, A.S. El-Demerdash, J Adv Vet Res **13**, 997 (2023)
3. A.T. Iacob, F.G. Lupascu, M. Apotrosoaei, I.M. Vasincu, R.G. Tauser, D. Lupascu, S.E. Giusca, I.D. Caruntu, L. Profire, Pharmaceutics (2021). https://doi.org/10.3390/pharmaceutics13040587
4. K. Divya, M.S. Jisha, Environ. Chem. Lett. (2018). https://doi.org/10.1007/s10311-017-0670-y
5. H.Y. Atay, *Antibacterial Activity of Chitosan-Based Systems* (2020)
6. H. Yilmaz Atay, in *Functional Chitosan: Drug Delivery and Biomedical Applications* (2020)
7. E.I. Rabea, M.E.T. Badawy, C.V. Stevens, G. Smagghe, W. Steurbaut, Biomacromol (2003). https://doi.org/10.1021/bm034130m
8. C.L. Ke, F.S. Deng, C.Y. Chuang, C.H. Lin, Polymers (Basel) **13**, 904 (2021)
9. M. Szulc and K. Lewandowska, Molecules **28**, (2023)
10. A.R. Egorov, A.A. Kirichuk, V.V. Rubanik, V.V. Rubanik, A.G. Tskhovrebov, A.S. Kritchenkov, Materials (2023). https://doi.org/10.3390/ma16186076
11. C. Ardean, C.M. Davidescu, N.S. Nemeş, A. Negrea, M. Ciopec, N. Duteanu, P. Negrea, D. Duda-seiman, V. Musta, Int. J. Mol. Sci. (2021). https://doi.org/10.3390/ijms22147449
12. M. Wypij, J. Trzcińska-Wencel, P. Golińska, G.D. Avila-Quezada, A.P. Ingle, M. Rai, Front. Chem. (2023). https://doi.org/10.3389/fchem.2022.1106230
13. C. Thambiliyagodage, M. Jayanetti, A. Mendis, G. Ekanayake, H. Liyanaarachchi, S. Vigneswaran, Materials (2023). https://doi.org/10.3390/ma16052073
14. E. Elashkar, R. Alfaraj, O.M. El-Borady, M.M. Amer, A.M. Algammal, A.S. El-Demerdash, Front. Microbiol. **15**, 1507274 (2024)
15. M.F. Saad, M.M. Elsayed, M. Khder, A.S. Abdelaziz, A.S. El-Demerdash, Sci. Rep. (2024). https://doi.org/10.1038/s41598-024-58349-4
16. M.T. Al-Shemy, A.S. El-Demerdash, A. Marzec, G.E. Dawwam, Int. J. Biol. Macromol. (2025). https://doi.org/10.1016/j.ijbiomac.2024.139012
17. P. Rahisuddin, S.A. AL-Thabaiti, Z. Khan, N. Manzoor, Bioproc. Biosyst. Eng. **38**, 1773–1781 (2015)
18. K. Maduray, R. Parboosing, Biol. Trace Elem. Res. (2021). https://doi.org/10.1007/s12011-020-02414-2
19. A. Sati, T.N. Ranade, S.N. Mali, H.K.A. Yasin, N. Samdani, N.N. Satpute, S. Yadav, A.P. Pratap, Molecules (2025). https://doi.org/10.3390/molecules30092004
20. Z.A. Ratan, F.R. Mashrur, A.P. Chhoan, S.M. Shahriar, M.F. Haidere, N.J. Runa, S. Kim, D.H. Kweon, H. Hosseinzadeh, J.Y. Cho, Pharmaceutics (2021). https://doi.org/10.3390/pharmaceutics13122034
21. M. Rybka, Ł Mazurek, M. Konop, Life **13**, 69 (2023)
22. B. Ahmed, A. Hashmi, M.S. Khan, J. Musarrat, Adv. Powder Technol. (2018). https://doi.org/10.1016/j.apt.2018.03.025
23. E.A. Kukushkina, S.I. Hossain, M.C. Sportelli, N. Ditaranto, R.A. Picca, N. Cioffi, Nanomaterials (2021). https://doi.org/10.3390/nano11071687
24. M.A. El-Meligy, E.M. Abd El-Monaem, A.S. Eltaweil, M.S. Mohy-Eldin, Z.M. Ziora, A. Heydari, A.M. Omer, Molecules (2024). https://doi.org/10.3390/molecules29102393
25. S.W. Ali, S. Rajendran, M. Joshi, Carbohydr. Polym. (2011). https://doi.org/10.1016/j.carbpol.2010.08.004
26. S. Magaldi, S. Mata-Essayag, C. Hartung De Capriles, C. Perez, M.T. Colella, C. Olaizola, Y. Ontiveros, Int. J. Infect. Dis. (2004). https://doi.org/10.1016/j.ijid.2003.03.002
27. W.M. Essawi, A.S. El-Demerdash, M.M. El-Mesalamy, M.A. Abonorag, Curr. Microbiol. **77**, 1399 (2020)
28. M.P. Spínola, A.R. Mendes, J.A.M. Prates, Foods (2024). https://doi.org/10.3390/foods13223656
29. A.H. Sewid, M. Sharaf, A.S. El-Demerdash, S.M. Ragab, F.O. Al-Otibi, M.T. Yassin, C.G. Liu, Front. Cell. Infect. Microbiol. (2025). https://doi.org/10.3389/fcimb.2024.1505469
30. M.A. Gamaleldin, A. Koriem, R. Hamed, S. Labib, A.S. El-Demerdash, Egypt. J. Vet. Sci. **0**, 1 (2025)

31. F.A. El-Shenawy, M.A.M. Kotb, D.M. Sharaf, A.S.E. El-Demerdash, World J. Microbiol. Biotechnol. (2025). https://doi.org/10.1007/s11274-025-04616-z
32. Z. Zhou, Y. Yang, L. He, J. Wang, J. Xiong, J. Mater. Sci. Mater. Med. (2022). https://doi.org/10.1007/s10856-022-06665-4
33. M. A. Khormi, M. A. Alfattah, M. A. Abo-Zaid, S. E. B. Abdalla, A. El-Shabasy, Asian J. Agricult. Biol. **2025**, (2025)
34. N.T. Phuong, V.A. Ho, D.H. Nguyen, N.C. Khoa, T.N. Quyen, Y. Lee, K.D. Park, J. Bioact. Compat. Polym. (2015). https://doi.org/10.1177/0883911515578760
35. N.T. Hiep, H.C. Khon, V.V.T. Niem, V.V. Toi, T.N. Quyen, N.D. Hai, M.N.T. Anh, Int. J. Polym. Sci. (2016). https://doi.org/10.1155/2016/1584046
36. A. M.-I. J. N. Chem and Undefined 2015, Naturalspublishing. Com **1**, (2015)
37. E. Mohsen, O.M. El-Borady, M.B. Mohamed, I.S. Fahim, J. Radiat. Res. Appl. Sci. (2020). https://doi.org/10.1080/16878507.2020.1748941
38. S. Akmaz, E. Dilaver Adgüzel, M. Yasar, O. Erguven, Adv. Mater. Sci. Eng. **2013**, (2013)
39. O.M. El-Borady, M.S. Ayat, M.A. Shabrawy, P. Millet, Adv. Powder Technol. (2020). https://doi.org/10.1016/j.apt.2020.09.017
40. K. Mallikarjuna, G. Narasimha, G. R. Dillip, B. Praveen, B. Shreedhar, C. Sree Lakshmi, B. V. S. Reddy, B. Deva Prasad Raju, Dig. J. Nanomater. Biostruct. **6**, (2011)
41. V.T. Le, L.G. Bach, T.T. Pham, N.T.T. Le, U.T.P. Ngoc, D.H.N. Tran, D.H. Nguyen, J. Macromol. Sci. A, Pure Appl. Chem. (2019). https://doi.org/10.1080/10601325.2019.1586439
42. O. Pawar, N. Deshpande, S. Dagade, S. Waghmode, P.N. Joshi, J. Exp. Nanosci. **11**, 28 (2016)
43. Z. Liu, Y. Wang, Y. Zu, Y. Fu, N. Li, N. Guo, R. Liu, Y. Zhang, Mater. Sci. Eng. C Mater. Biol. Appl. (2014). https://doi.org/10.1016/j.msec.2014.05.007
44. L. Biao, S. Tan, Y. Wang, X. Guo, Y. Fu, F. Xu, Y. Zu, Z. Liu, Mater. Sci. Eng. C Mater. Biol. Appl. (2017). https://doi.org/10.1016/j.msec.2017.02.154
45. V.K. Lamer, R.H. Dinegar, J. Am. Chem. Soc. (1950). https://doi.org/10.1021/ja01167a001
46. Y. Xia, Y. Xiong, B. Lim, S.E. Skrabalak, Angew. Chem. Int. Ed. (2009). https://doi.org/10.1002/anie.200802248
47. Y. Wu, D. Wang, Y. Li, Sci. China Mater. (2016). https://doi.org/10.1007/s40843-016-5112-0
48. A. Kirakosyan, J. Kim, S.W. Lee, I. Swathi, S.G. Yoon, J. Choi, Cryst. Growth Des. (2017). https://doi.org/10.1021/acs.cgd.6b01648
49. B. Abebe, D. Tsegaye, H.C. Ananda Murthy, RSC Adv. (2022). https://doi.org/10.1039/D2RA05222A
50. R. Prasad, R. Pandey, I. Barman, WIREs Nanomed. Nanobiotechnol. (2016). https://doi.org/10.1002/wnan.1363
51. B. Wang, K. Chen, S. Jiang, F. Reincke, W. Tong, D. Wang, C. Gao, Biomacromol (2006). https://doi.org/10.1021/bm060030f
52. E. Padan, Biochim Biophys Acta Bioenerg **1837**, (2014)
53. J.A. Malik, R. Lone, Mol. Biol. Rep. (2021). https://doi.org/10.1007/s11033-021-06676-4
54. J. Ståhle, G. Widmalm, Trends Glycosci. Glycotechnol. (2019). https://doi.org/10.4052/tigg.1749.7J
55. H. Murata, R.R. Koepsel, K. Matyjaszewski, A.J. Russell, Biomaterials (2007). https://doi.org/10.1016/j.biomaterials.2007.06.012
56. K.B. Holt, A.J. Bard, Biochemistry (2005). https://doi.org/10.1021/bi0508542
57. A. Dror-Ehre, H. Mamane, T. Belenkova, G. Markovich, A. Adin, J. Colloid Interface Sci. (2009). https://doi.org/10.1016/j.jcis.2009.07.052
58. N.L. Martin, P. Bass, S.N. Liss, PLoS ONE **10**, e0131345 (2015)
59. P. Kaur, A. Choudhary, R. Thakur, Int. J. Sci. Eng. Res. **4**, 869 (2013)
60. M.E.I. Badawy, T.M.R. Lotfy, S.M.S. Shawir, Bull. Natl. Res. Cent. (2019). https://doi.org/10.1186/s42269-019-0124-8
61. R. Kalaivani, M. Maruthupandy, T. Muneeswaran, A. Hameedha Beevi, M. Anand, C.M. Ramakritinan, A.K. Kumaraguru, Front. Lab. Med. (2018). https://doi.org/10.1016/j.flm.2018.04.002
62. B. Ahmad, L. Chang, C. Yin, Z. Wu, A. Tong, C. Tong, B. Liu, Nanomaterials (2024). https://doi.org/10.3390/nano14030237
63. L. Chang, B. Ahmad, A. Tong, Z. Wu, P. Xu, Z. Gao, C. Yin, M. Luan, C. Tong, B. Liu, Int. J. Biol. Macromol. **315**, 144222 (2025)
64. M.A. Wahab, L. Li, H. Li, A. Abdala, Nanomaterials (2021). https://doi.org/10.3390/nano11030581
65. S. Alfei, A.M. Schito, Pharmaceuticals **15**, 476 (2022)
66. A. S. El-Demerdash, R. M. Orady, A. A. Matter, and A. F. Ebrahem, Indian J. Microbiol. **1**, (2023)
67. A.S. El-Demerdash, S.A. Kamel, E.Y.T. Elariny, H. Henidi, Y. Mahran, H. Alahdal, A.M. Saleh, R.A. Ibrahim, Int. J. Mol. Sci. (2024). https://doi.org/10.3390/ijms252312949
68. E. Pradel, J.M. Pagès, Antimicrob. Agents Chemother. (2002). https://doi.org/10.1128/AAC.46.8.2640-2643.2002
69. H. Ogasawara, T. Ishizuka, S. Hotta, M. Aoki, T. Shimada, A. Ishihama, Microbiology (2020). https://doi.org/10.1099/mic.0.000947
70. A.S. El-Demerdash, A.E. Sehim, A. Altamimi, H. Henidi, Y. Mahran, G.E. Dawwam, Microorganisms **13**, 1818 (2025)
71. A.F. Ebrahem, A.S. El-Demerdash, R.M. Orady, N.M. Nabil, Probiotics Antimicrob. Proteins **16**, 1087 (2024)
72. E. Kaplan, N.P. Greene, A. Crow, V. Koronakis, Proc. Natl. Acad. Sci. U S A **115**, E7389–E7397 (2018)